Structural modifications of low-energy heavy-ion irradiated germanium

T. Steinbach,[1] J. Wernecke,[1] P. Kluth,[2] M. C. Ridgway,[2] and W. Wesch[1]

[1]*Institut für Festkörperphysik, Friedrich-Schiller-Universität Jena, Max-Wien-Platz 1, D-07743 Jena, Germany*
[2]*Australian National University, Research School of Physics and Engineering, Canberra, Australia*

Heavy-ion irradiation of crystalline germanium (c-Ge) results in the formation of a homogeneous amorphous germanium (a-Ge) layer at the surface. This a-Ge layer undergoes structural modification such as a strong volume expansion accompanied by drastic surface blackening with further ion irradiation. In the present paper we investigate the mechanism of this ion-induced structural modification in a-Ge basically for the irradiation with I ions (3 and 9 MeV) at room and low temperature as a function of ion fluence for the ion incidence angles of $\Theta = 7°$ and $\Theta = 45°$. For comparison, Ag- and Au-ion irradiations were performed at room temperature as a function of the ion fluence. At fluences two orders of magnitude above the amorphization threshold, morphological changes were observed for all irradiation conditions used. Over a wide range of ion fluences we demonstrate that the volume expansion is caused by the formation of voids at the surface and in the depth of the projected ion range. At high ion fluences the amorphous layer transforms into a porous structure as established by cross section and plan view electron microscopy investigations. However, the formation depth of the surface and buried voids as well as the shape and the dimension of the final porous structure depend on the ion fluence, ion species, and irradiation temperature and will be discussed in detail. The rate of the volume expansion (i.e., porous layer formation) depends linearly on the value of ϵ_n. This clearly demonstrates that the structural changes are determined solely by the nuclear energy deposited within the amorphous phase. In addition, at high ion fluences all perpendicular ion irradiations lead to a formation of a microstructure at the surface, whereas for nonperpendicular ion irradiations a nonsaturating irreversible plastic deformation (ion hammering) without a microstructure formation is observed. For the irradiation with ion energies of several MeV, the effect of plastic deformation shows a linear dependence on the ion fluence. Based on these results, we provide an explanation for the differences in surface morphology observed for different angles of incidence of the ion beam will be discussed in detail.

I. INTRODUCTION

In many crystalline semiconductors ion irradiation with energies of several hundred keV (energy transfer to lattice atoms of a few keV nm^{-1}, nuclear energy deposition, ϵ_n) results in amorphization of the material at certain ion fluences. In some semiconductors [e.g., GaSb (Refs. [1–5]), InSb (Refs. [6–8]), and Ge (Refs. [9–17])] further irradiation leads to void formation within the amorphous layer and transformation to a porous structure close to the sample surface. The properties of porous semiconductors may differ significantly from their corresponding bulk materials. The utilization of such differences promotes the application of porous structures in advanced technologies. Possible applications of porous semiconductors can be found in gas sensors,[18] templates,[19] filters,[20] as well as in fuel cells,[21] photonic crystals,[22] and solar cells.[23]

The first to observe morphological changes in Ge was Wilson.[9] He reported a crystalline-to-amorphous transformation at an ion fluence of $N_I \approx 10^{14}$ cm^{-2}, followed by the formation of surface craters at $N_I \approx 10^{15}$ cm^{-2} in amorphous germanium (a-Ge), which evolved into a cellular surface structure for ongoing irradiation. Holland and Appleton[10,11] observed a blackening of irradiated (111) and (110) Ge samples as a first sign of surface changes for $N_I > 10^{15}$ cm^{-2}. Furthermore, *ex situ* Rutherford backscattering spectrometry (RBS) analysis showed a large yield deficit near the surface compared to the random spectrum for both orientations of Ge. Electron microscopy investigations revealed a porous honeycomb layer

with a thickness much larger than the projected ion range beneath the surface as a reason for the surface blackening and the deficit of the RBS yield. This drastic morphological change had been demonstrated previously in a-Ge irradiated at room temperature (RT) with a variety of heavy ions (Ge, As, Kr, In, Sb, Xe,W Pb, Sn, Tl, and Bi) (see Refs. [9–17] and references therein), but not for light ions such as He, F, and Si (Ref. [12]). In the case of irradiations at liquid nitrogen temperature (LNT), a slight blackening at $N_I \approx 3 \times 10^{16}$ cm^{-2} indicated structural changes in Ge as well.[12] Furthermore, it was reported that a free surface is not necessary for crater formation as irradiation of a-Ge samples covered with a thin aluminium[12] or silicon dioxide[15] surface layer on top also exhibited a honeycomb structure. Based on the observations mentioned above, Appleton *et al.* concluded that for the onset of morphological changes a critical defect production rate is necessary (ion mass dependence), void formation may be a defect-driven phenomenon (temperature dependence) and voids only evolve within the amorphous phase. Wang and Birtcher[13] thermally annealed the irradiated porous samples to achieve recrystallization. While the amorphous part of Ge became crystalline again, the porous structure remained almost unchanged, even after annealing at 940 K. As a driving formation mechanism they proposed the minimization of dangling Ge bonds at void surfaces. Stritzker *et al.*[14] examined the volume expansion of self-ion irradiated Ge at different temperatures and showed that pronounced swelling and blackening of the samples were observed exclusively in

a temperature regime of 200 to 500 K. Below and above this temperature regime, only sputter erosion without swelling was registered up to $N_I = 1 \times 10^{17}$ cm^{-2}. It was concluded that below 200 K, the temperature is too low for vacancy diffusion and clustering, whereas above 200 K, vacancies are sufficiently mobile to cluster and form voids. For irradiation at T > 500 K, the recombination of Frenkel pairs is thermally activated and the irradiated layer remains crystalline.[14,24]

A similar volume expansion and porous structure formation can be observed for high-energy heavy-ion irradiation (swift heavy ion (SHI) with kinetic energies above one hundred MeV),[25–27] where the dominant stopping process is the inelastic interaction of ions with target atoms, known as electronic energy deposition ϵ_e, with values of $\approx$ 10–60 keV nm^{-1}. More recently, the influence of ϵ_e on void formation as well as the plastic deformation in SHI irradiated a-Ge layers was investigated.[27] An electronic energy deposition threshold for void formation could be determined ($\epsilon_e = 10.5$ keV nm^{-1}). To get a deeper insight into the process of void formation due to SHI irradiation we have investigated the effect by means of molecular dynamics (MD) computer simulations, which clearly demonstrate that the experimentally proven void formation in SHI irradiated a-Ge can be explained by a shock wave mechanism as a result of the high electronic energy deposition.[28] Furthermore, nonperpendicular SHI irradiation of a-Ge leads to fluence-dependent plastic flow in the direction of the ion beam projection on the surface.[26,27]

The purpose of the present paper is to investigate the mechanism of porous layer formation in Ge basically for the irradiation with I ions at room and low temperature as a function of ion fluence for the ion incidence angles of $\Theta = 7°$ and $\Theta = 45°$. To separate the maximum of ϵ_e and ϵ_n as well as to increase the penetration depth, irradiations were performed with ion energies in the range of several MeV. For the I irradiation, we present ion-induced morphological changes in Ge over a wide range of ion fluence, beginning with the amorphization process of crystalline germanium (c-Ge), followed by the formation of voids in the amorphous phase and its transformation into a porous structure at high fluences. For comparison with the I irradiation, Ag- and Au-ion irradiations were performed at room temperature as a function of the ion fluence. The Ag- and Au-ion energy was adjusted to achieve similar depth distributions and maximal penetration depths for all ion species used. Depending on the ion fluence, different stages of porous layer formation are observed and

we could demonstrate that the rate of the volume expansion depends only on ϵ_n. However, the formation depth of the voids depends on the ion species used (chemical properties of the irradiated ions), whereas the shape and the dimension of the porous structure shows a strong dependence on the irradiation temperature. In addition, for all perpendicular ion irradiations, a formation of a microstructure at the surface occurs, whereas for nonperpendicular ion irradiation a plastic deformation without a microstructure formation was observed. The effect of plastic deformation as well as an explanation for the differences in surface morphology observed for different angles of incidence of the ion beam will be discussed in detail.

II. EXPERIMENT

Crystalline germanium (c-Ge, [100] orientation) samples were irradiated with heavy ions having kinetic energies in the range of $E = 3$–9 MeV. To quantify the swelling of the sample, one half was masked with an aperture, which inhibits ion penetration to allow the comparison of irradiated and unirradiated material. The samples were kept at room temperature (RT) and the irradiation was performed at tilt angles of $\Theta = 7°$ and $45°$ with respect to the crystal axis [100]. In addition, to elucidate the influence of thermally induced defect mobility on the void formation, irradiations at liquid nitrogen temperature (LNT) have been performed. The ion fluence N_I ranged between 5×10^{11} cm^{-2} and 1×10^{17} cm^{-2}. Table I summarizes details of the ion irradiation conditions as well as the values of ϵ_n and ϵ_e taken in the maximum of the distributions, the number of primary displaced lattice atoms N_{displ} and the projected ion range as estimated by SRIM 2008 calculations.[29] Figure 1 shows, as an example, the calculated depth profiles of ϵ_n and ϵ_e as well as the ion distribution for irradiation of 3 and 9 MeV iodine ions in a-Ge ($\Theta = 7°$).

Rutherford backscattering spectrometry (RBS) in channeling configuration (RBS/C) with 2.0 MeV He$^+$ ions and a backscattering angle of 170° was carried out to analyze the damage accumulation. The relative concentration of displaced lattice atoms $n_{da}(z)$ as a function of depth z was calculated using the computer code DICADA, which is based on the discontinuous model of dechanneling.[30,31] In the following n_{da} is referred to as defect concentration, in which $n_{da} = 0$ and 1 correspond to perfect crystals and amorphous material, respectively. The ion-induced swelling of the irradiated areas was measured relative to the unirradiated surface parts with a

TABLE I. Conditions of the ion irradiations performed with an ion flux of approximately 1×10^{12} cm^{-2} s^{-1}, where E, m, Θ, T, and N_I denote the ion energy, the ion mass, the angle of incidence with respect to the surface normal, the irradiation temperature, and the ion fluence range, respectively. In addition, the calculated values (SRIM 2008[29]) of the electronic and nuclear energy deposition $\epsilon_{e,n}$, the primary displaced lattice atoms N_{displ}, as well as the projected ion range R_p are given.

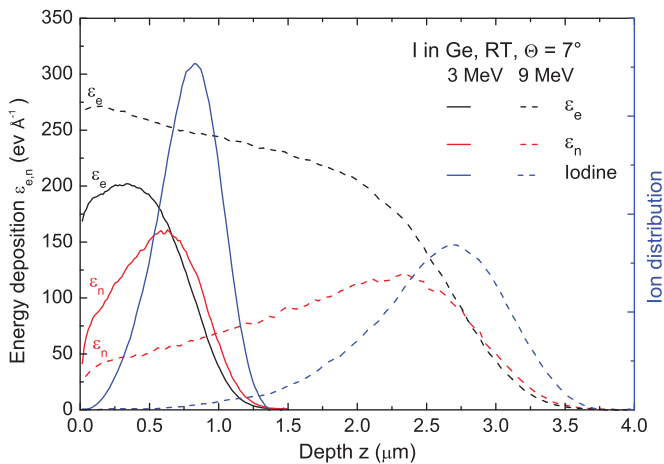| Ion	E (MeV)	m (amu)	Θ (°)	ϵ_e (eV Å^{-1})	ϵ_n	T	N_{displ} (ion^{-1} Å^{-1})	R_p (nm)	N_I (cm^{-2})
Ag	2.5	107.9	7	167.1	138.7	RT	6.9	810	1×10^{15}–5×10^{16}
I	3.0	126.9	7	201.0	161.3	RT/LNT	9.5	835	5×10^{11}–9×10^{16}
I	3.0	126.9	45	296.6	212.1	RT/LNT	10.6	555	5×10^{11}–9×10^{16}
I	9.0	126.9	7	271.1	120.9	RT	6.4	2700	1×10^{15}–5×10^{15}
Au	4.5	197.0	7	352.2	261.5	RT	12.9	770	1×10^{15}–8×10^{16}

FIG. 1. (Color online) SRIM calculation (Ref. 29) of the electronic ϵ_e and the nuclear ϵ_n energy deposition as well as the iodine distribution versus depth z for germanium irradiated with 3 and 9 MeV I ions.

Sloan DEKTAK 3030ST surface profilometer, which achieves a vertical resolution of several nanometers. To quantify the surface roughness, atomic force microscopy (AFM, VEECO MultiMode AFM) with a subnanometer resolution was used. Additionally, scanning electron microscopy (SEM) and transmission electron microscopy (TEM) were applied to gain structural information. SEM was used in plan-view (pv-SEM) as well as in cross-section (cs-SEM) geometry. The images were taken at a Zeiss UltraPlus analytical FESEM and a JEOL 7001F SEM with a typical acceleration voltage of 10 kV. The cross-sectional TEM (cs-TEM) samples were prepared using standard techniques such as mechanical grinding and polishing followed by low angle Ar ion etching. TEM images were taken at a JEOL JEM-3010 TEM with a LaB$_6$ cathode and an acceleration voltage of 300 kV.

III. RESULTS

A. Defect formation: Crystalline-amorphous transition

Figure 2(a) shows the defect concentration n_{da} as determined from RBS/C measurements as a function of depth z for room temperature irradiation of c-Ge with 3 MeV I ions and $\Theta = 7°$ at different ion fluences. It can be seen that with rising ion fluence the defect concentration increases. The defect maximum ($z = 575$ nm) is located in the depth of the nuclear energy deposition (cf. Fig. 1). The depth profiles (depth of the defect maximum and shape of the profiles) are in good agreement with the calculated curve of N_{displ} [dashed black line in Fig. 2(a)]. The electronic energy deposition itself is too low in this energy regime to produce significant defects in semiconductors[27,32] and can be neglected.

In Fig. 2(b), the defect concentration determined in the maximum of the defect profiles, n_{da}^{max}, is given as a function of fluence. Numerous models[33–39] were developed to describe the fluence dependence of the defect concentration. The data in Fig. 2 can be fitted in the framework of a modified Hecking model.[38] This model assumes a direct impact damage with a cross section P_a and stimulated growth of amorphous regions
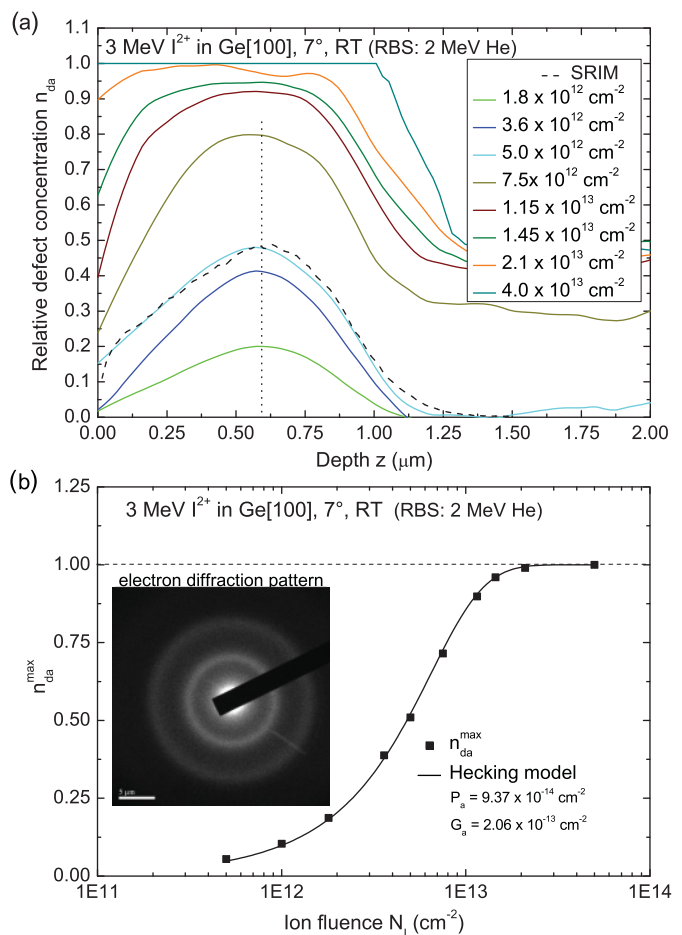

FIG. 2. (Color online) (a) Relative defect concentration n_{da} versus depth z for Ge irradiated at room temperature with 3 MeV I ions under an incidence angle of $\Theta = 7°$. The primary displacements, N_{displ}, [black dashed line, SRIM 2008 (Ref. 29) calculation] is given for comparison in arbitrary units. (b) Relative defect concentration in the maximum of the distribution n_{da}^{max} as a function of the ion fluence. The fit (black line) accounts for direct impact amorphization and stimulated growth of already existing amorphous regions (Hecking model) (Ref. 38). The inset of (b) shows an electron diffraction pattern of the irradiated surface layer ($N_I = 4.0 \times 10^{13}$ cm^{-2}).

G_a, which exist from previous ion impacts (n_a, relative amount of defects)

$$\frac{dn_a}{dN_I} = (P_a + G_a n_a)(1 - n_a). \tag{1}$$

At the beginning of the irradiation (i.e., for low ion fluences) each ion hits still crystalline material and the collision cascades of single ions do not overlap. Hence, the defect concentration is controlled by the parameter P_a, which quantifies the influence of individual ion impact in unirradiated material. Stimulated amorphization begins if the collision cascades start to overlap and becomes dominant at higher fluences. The amorphization in the defect maximum (i.e., $n_{da} = 1$) is reached at an amorphization fluence of approximately $N_I^{am} = 2 \times 10^{13}$ cm^{-2}. In this case, the normalized ion fluence (i.e., the number of displacements per lattice atom $n_{dpa} = N_{displ} N_I^{am}/N_0$ with the atomic density $N_0 = 4.41 \times 10^{22}$ cm^{-3}) amounts to $n_{dpa} = 0.44$ dpa.

Based on the high values of P_a and G_a [see Fig. 2(b)], it can be concluded that a direct impact amorphization in c-Ge takes place even at room temperature ion irradiation. Moreover, using MD simulations Nordlund *et al.* showed for Ge that recoils of several keV cause large molten regions in the material followed by amorphization of these regions due to rapid cooling.[40] Collision cascades in Si are characterized by lower density and consequently less damaged regions with a higher proportion of isolated defects are formed.[40] According to Impellizzeri *et al.* the higher damage rate of Ge compared to Si may be attributed to a higher stopping power of Ge atoms and a lower mobility of defects within the collision cascades.[41]

With further increasing ion fluence, $N_I > 2 \times 10^{13}$ cm^{-2}, the amorphous region broadens toward the surface and into the depth [see Fig 2(a)]. Consequently, for high ion fluences, a homogeneous amorphous surface layer has formed with thickness d_{RBS} (e.g., $d_{RBS} = 1$ μm at $N_I = 4 \times 10^{13}$ cm^{-2}). This is also confirmed by the occurrence of diffuse rings of the electron diffraction patterns as depicted in the inset of Fig. 2(b), which reveals that the surface layer is completely amorphous (sample irradiated to $N_I = 4 \times 10^{13}$ cm^{-2}).

In summary, the threshold fluence for amorphization of c-Ge at RT with heavy ions and energies as mentioned in the previous section is found to be in the range of 10^{13} cm^{-2}. For LNT irradiation, the amorphization fluence decreases[34,38] because intrinsic defects may become immobile and thermal effects like the defect recombination within the primary collision cascades, which reduces the damage remaining after irradiation, can be excluded (see Ref. 42 and references therein). Altogether, it can be concluded that the amorphization of Ge takes place in an ion fluence range which is more than two orders of magnitude below the fluences relevant for morphological changes.[9–17] The step height, which quantifies the swelling due to void formation, is measured relative to the unirradiated surface areas (i.e., the crystalline surface). However, the mechanically constrained density change due to the amorphization which leads to a visible elevation of the surface has to be considered in the discussion of the swelling due to void formation.

In Fig. 3 the measured step height caused by amorphization Δz^{am} is depicted as a function of ion fluence for the irradiation of c-Ge with 3 MeV I ions and incidence angles of $\Theta = 7°$ and $45°$, respectively. With increasing ion fluence [i.e., increasing defect formation (cf. Fig. 2)] Δz^{am} increases until a saturation step height of about 35 and 20 nm for $\Theta = 7°$ and $45°$ is reached, respectively (cf. Fig. 3, a-Ge). At this fluence range a homogeneous amorphous surface layer has formed (cf. Fig. 2). With further irradiation, Δz^{am} increases slightly, which can be seen in Fig. 3 and may be attributed to the increase in the thickness of the amorphous layer. Cs-TEM investigations of these layers ($N_I = 5$–10×10^{14} cm^{-2}) confirmed that they are homogeneous and free of voids and cavities. Based on the step height measurements and the thickness of the amorphous layer determined from the TEM analysis, a density decrease of $\Delta\rho = \Delta z^{am}/d_{TEM} = 3.2\%$ is obtained. This is in good agreement with the values reported in the literature.[43–45] Extended x-ray absorption fine structure (EXAFS) studies of amorphized Ge performed by different groups[46,47] also confirm a volume density decrease by 1% to 3% as a result of bond
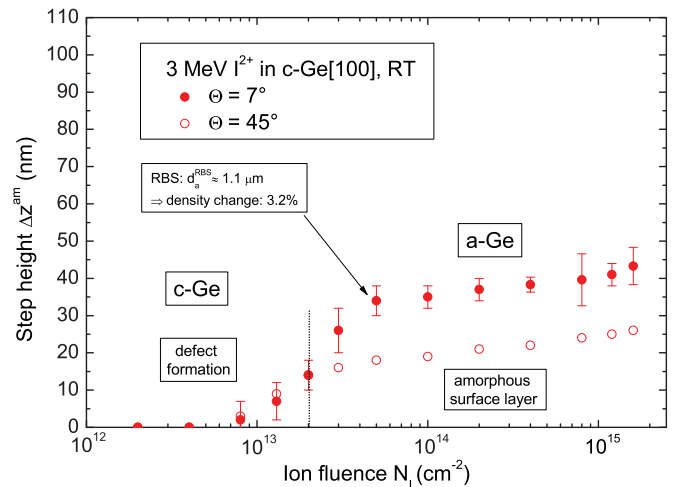

FIG. 3. (Color online) Mean step height Δz^{am} of the surface of ion irradiated germanium with respect to the corresponding unirradiated part as a function of the ion fluence N_I. The irradiations were carried out at room temperature with 3 MeV I ions under an angle of $\Theta = 7°$ and $45°$, respectively.

length expansion due to amorphization by ion bombardment of c-Ge.

B. Ion-beam-induced porosity

1. Volume expansion

At ion fluences above 2×10^{15} cm^{-2}, an extreme ion-beam-induced swelling Δz occurs, as shown in Fig. 4 for RT irradiation with 3 and 9 MeV I ions at $7°$ and $45°$ ion incidence, respectively. The fluence dependence of the step height exhibits three distinct regions (I–III) characterized by different slopes of the curves (cf. Table II). The step height
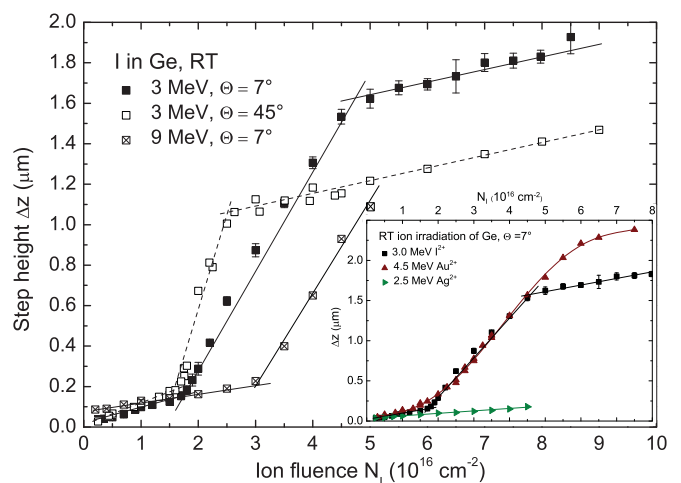

FIG. 4. (Color online) Mean step height Δz of the surface as a function of the ion fluence N_I for room temperature irradiated germanium with 3 and 9 MeV I ions under an angle of $\Theta = 7°$ and $45°$, respectively. The lines are linear approximations indicating three different regions along the fluence axis. The inset shows the step height Δz for Ge irradiated with 4.5 MeV Au and 2.5 MeV Ag in comparison to the 3 MeV I-irradiation as a function of fluence N_I (for all $\Theta = 7°$).

TABLE II. Overview of the threshold fluences and slopes of the different step height regions for all irradiation conditions, including the appearance of the sample surface after irradiation.

Region	Irradiation conditions	Threshold fluence (10^{16} cm^{-2})	Slope (nm / 10^{16} cm^{-2})	Surface blackening
I	3 MeV, 7°	0.25	86.2	onset of blackening, shiny surface
	3 MeV, 45°	0.2	118.1	
	9 MeV, 7°	0.4	47.4	
II	3 MeV, 7°	1.7	485.3	black, but shiny surface
	3 MeV, 45°	1.55	837.5	
	9 MeV, 7°	2.8	458.6	
III	3 MeV, 7°	4.75	71.8	matte and grained, silvery surface
	3 MeV, 45°	2.6	68.0	black, but shiny surface (like II)
	9 MeV, 7°	>5		

increases linearly with a small slope in region I, followed by a steeper slope in region II, until the gradient levels again in region III. In the case of 9 MeV I-ion irradiation, only regions I and II were observed, which can be attributed to the relatively low final ion fluence. In addition, at the lowest ion fluence, Δz is approximately three times larger compared to the irradiation with 3 MeV due to the increased thickness of the amorphous layer at 9 MeV. Table II gives an overview of the threshold fluences and slopes of the different regions for all irradiation conditions. It is obvious, that the threshold fluences decrease with increasing energy depositions (cf. Tables I and II). That means, the higher the energy deposition, the smaller the fluence necessary to reach the same total energy deposition. Furthermore, the projected ion range R_p of 3 MeV I ions, $\Theta = 45°$, is closer to the surface compared to an incidence angle of 7°, which causes a lower saturation step height at high fluences (region III). The ratio of saturation step height and R_p as derived from SRIM calculations[29] for the two angles of incidence (see Table I)

$$\text{saturation step height} : \frac{\Delta z^{7°}}{\Delta z^{45°}} = \frac{1.67\,\mu\text{m}}{1.12\,\mu\text{m}} = 1.49, \quad (2)$$

$$\text{ion range} : \frac{R_p^{7°}}{R_p^{45°}} = \frac{835\,\text{nm}}{555\,\text{nm}} = 1.50, \quad (3)$$

are in good agreement with each other. Thus, the differences in saturation step height and threshold fluence at different irradiation conditions are a result of different energy depositions and ion ranges. It can also be noted that the changes in appearance of the sample surface after irradiation as described in the right column in Table II indicate a strong correlation between surface color changes and the transitions between the regions. Moreover, for identical irradiation conditions, the swelling Δz is well reproducible within experimental uncertainty.

The inset of Fig. 4 shows the volume expansion of Ge samples irradiated with 4.5 MeV Au and 2.5 MeV Ag in comparison to the 3 MeV I irradiation as a function of fluence ($\Theta = 7°$ in all cases). The ion energy was adjusted to achieve similar depth distributions and maximal penetration depths (approximately 1 μm) for all ion species. Consequently, the thickness of the amorphized material which becomes porous is comparable. For irradiation with Ag even at the highest ion fluence of $N_I = 4.5 \times 10^{16}$ cm^{-2} the step height reaches

a value of only $\Delta z = 180$ nm, and there is no transition from region I to region II. In contrast, the irradiation with Au clearly leads to a strong volume expansion like the 3 MeV I irradiation. However, Δz shows no sharp transition between the three regions as observed for all irradiations with iodine. The transition for the Au irradiation seems to be rather continuous. In addition, the appearance of the sample surface after irradiation changed with increasing ion fluence from black to matte and silvery, corresponding to iodine irradiation (cf. Table II).

2. Void and porous layer formation

A cs-TEM view of a sample irradiated with 1.2×10^{16} cm^{-2} (3 MeV I ions, $\Theta = 7°$: region I) is depicted in Fig. 5(a), which reveals the formation of a distinct porous layer at the surface. A magnification of the porous surface structure clearly shows the nanoporous, columnar-shaped structure with a height of 130 nm, column diameters of 10 to 30 nm, and walls with a thickness of approximately 5 nm. Underneath, a 1.5-μm thick amorphous layer without any inner structure or other features is present. Every TEM and SEM image taken at samples irradiated with fluences within region I shows that the porous layer formation begins at the surface and expands in the underlying a-Ge layer with increasing N_I. At $N_I = 1.7 \times 10^{16}$ cm^{-2}, a few buried isolated spherical voids were formed within the previously featureless amorphous Ge layer, having sizes of 5 to 13 nm and an average distance of about 800 nm (not shown). With increasing N_I the void density and void dimension of this buried voids increases which is demonstrated in Fig 5b, in which a cs-SEM image of a sample representative for the transition between regions I and II, $N_I = 1.8 \times 10^{16}$ cm^{-2}, is shown. In a depth z_b a buried void-rich band is clearly visible with void dimensions of 5 to 25 nm. Independent of E and Θ, all samples irradiated with iodine ions show the same qualitative behavior in regions I and II. With respect to the initial, crystalline surface, z_b amounts to 825 nm [3 MeV, $\Theta = 7°$, Fig. 5(b)], 550 nm (3 MeV, $\Theta = 45°$), and 2600 nm (9 MeV, $\Theta = 7°$). Hence, z_b is larger than the depth of the nuclear energy deposition maximum and therefore larger than the depth of the defect maximum [cf. Figs. 1 and 2(a)]. Thus, for all I irradiations, the buried voids are located in the depth of R_p (cf. Table I), with respect to the initial surface.
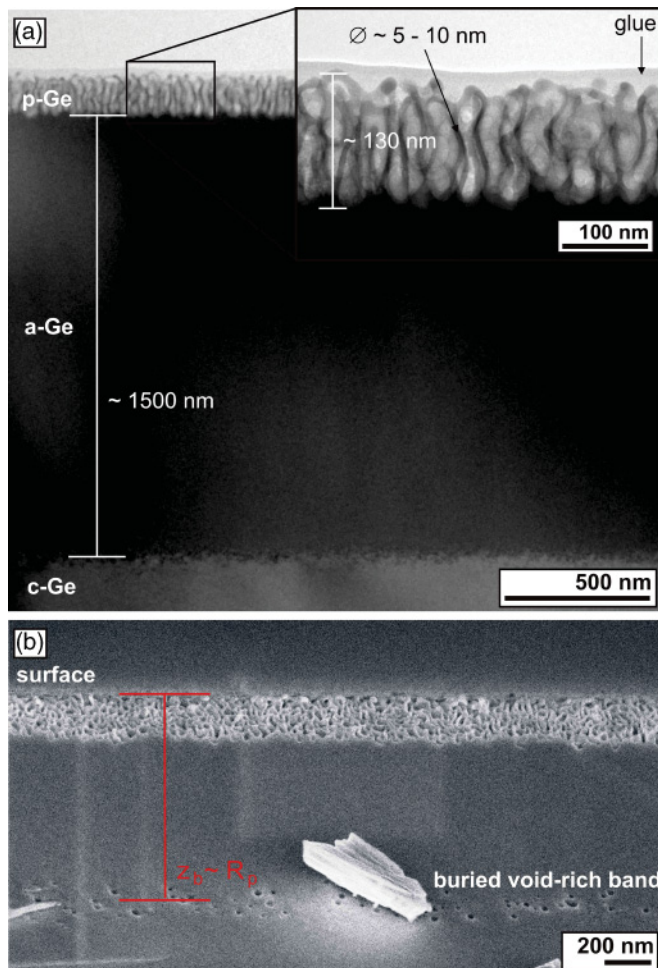
FIG. 5. (Color online) The cs-TEM image in (a) shows the formation of a nanoporous, columnar-shaped structure at the surface and a 1.5-μm thick amorphous layer without any inner structure underneath after the irradiation with 3 MeV I ions under an angle of $\Theta = 7°$ with an ion fluence of 1.2×10^{16} cm^{-2} (region I). The formation of buried void-rich band within the previously featureless amorphous Ge layer is shown in (b) for a sample irradiated with 3 MeV I ions under an angle of $\Theta = 7°$ with an ion fluence of 1.8×10^{16} cm^{-2} (transition between regions I and II).

Ongoing irradiation leads to the formation of a buried porous layer and broadening of both, surface and buried porous layer. This is verified by the cs-TEM image of a sample irradiated to $N_I = 4.0 \times 10^{16}$ cm^{-2} as depicted in Fig. 6. The image of the complete layer structure [Fig. 6(a)] demonstrates the sharp transitions between porous surface, amorphous interlayer, porous buried layer, underlying amorphous region, and amorphous-crystalline transition zone. The abrupt changes in the transition point to sharp thresholds and a homogeneous formation process. A magnification of the buried structure with a thickness of 1.6 μm is shown in Fig. 6(c). Apparently, it consists of randomly distributed bubble-shaped cavities with diameters ranging from several tens of nanometers up to a hundred nanometers. Diffuse rings in electron diffraction patterns of the cell walls with a thickness of around 5 nm indicate that they consist of a-Ge. In comparison, the surface

layer with a thickness of 540 nm [Fig. 6(b)] has a similar wall thickness and void dimension, but seems to be more stretched into a columnar structure. In addition, electron diffraction patterns of these walls as well as the amorphous interlayer and underlying amorphous region did not differ from the pattern displayed in the inset of Fig. 6(c). Thus, these structures also consist of a-Ge. A magnified view of the sharp transition between the buried porous layer and the underlying amorphous layer as well as the amorphous layer and the crystalline substrate is depicted in Fig. 6(d). Based on Fig. 6, it can be seen that mainly the buried layer expands, thus, being primarily responsible for the steep slope in region II.

In region III surface and buried porous layers grow together with increasing N_I. This is illustrated in Fig. 7(a) for $N_I = 5 \times 10^{16}$ cm^{-2} where both porous layers are still separated by a thin a-Ge layer. At $N_I = 7 \times 10^{16}$ cm^{-2}, finally, only one continuous porous layer is observed [Fig. 7(b)]. In this case the structure of the layer varies from cavities at the surface which are more stretched toward the surface to a more bubble-like structure at the porous-amorphous interface, which is still very sharp as also observed in region II.

As an example, Fig. 8 shows Δz compared to the thickness of the porous surface layer, the amorphous interlayer, as well as the porous buried layer as determined by means of the cs-SEM and TEM images as a function of N_I for the irradiation with 3 MeV I at $\Theta = 7°$. In region I, Δz increases as a result of the formation and growth of a porous layer at the surface. Above $N_I = 1.7 \times 10^{16}$ cm^{-2} the increase in Δz is dominated by the formation and expansion of a buried porous layer, whereas the amorphous interlayer between these porous structures continuously decreases.

With this data, a rough estimate of the relative change in density $\alpha = d_a/d_p$ can be made, where d_p is the complete porous layer thickness (surface layer + buried layer) and d_a refers to the original amorphous material that became porous during the irradiation, $d_a = d_p - \Delta z_p$. The amorphization-induced elevation, Δz^{am}, which dominates at low N_I was considered as follows: $\Delta z_p = \Delta z - \Delta z^{am}$. The opposing effect of sputter erosion due to ion bombardment results for irradiation with 3 MeV I, $\Theta = 7°$ and $N_I = 1 \times 10^{16}$ cm^{-2} in a sputtered depth of 8 nm (sputter rate $r_s = 3.41$ atoms ion^{-1}, SRIM 2008.[29]) Hence, at ion fluences in the range of 0.1 to 3×10^{16} cm^{-2} the amorphization-induced swelling ($\Delta z^{am} \approx 35$ nm) dominates and the sputter effect can be neglected. At $N_I > 3 \times 10^{16}$ cm^{-2}, sputtering effectively compensates amorphization-induced swelling and both effects can be neglected within experimental uncertainty. The factor α is depicted as a function of N_I in the inset of Fig. 8. It can bee seen that α decreases continuously with increasing N_I and saturates at high ion fluences in the range of 0.40 to 0.37 (but still decreases slightly with increasing N_I). In other words, the thickness of the original amorphous material is around 38% of the porous material. The large error bars at low fluences are attributed to the large error caused by the step height measurements as well as the thickness determination (d_p) of the initially thin porous layer. In addition, the small increase in α within the fluence range of $N_I = 1.7$ to 2.0×10^{16} cm^{-2} (i.e., transition from region I to region II) is also attributed to the difficult estimation of d_p for the new formed buried porous layer [cf. Fig. 5(b)]. Obviously, we
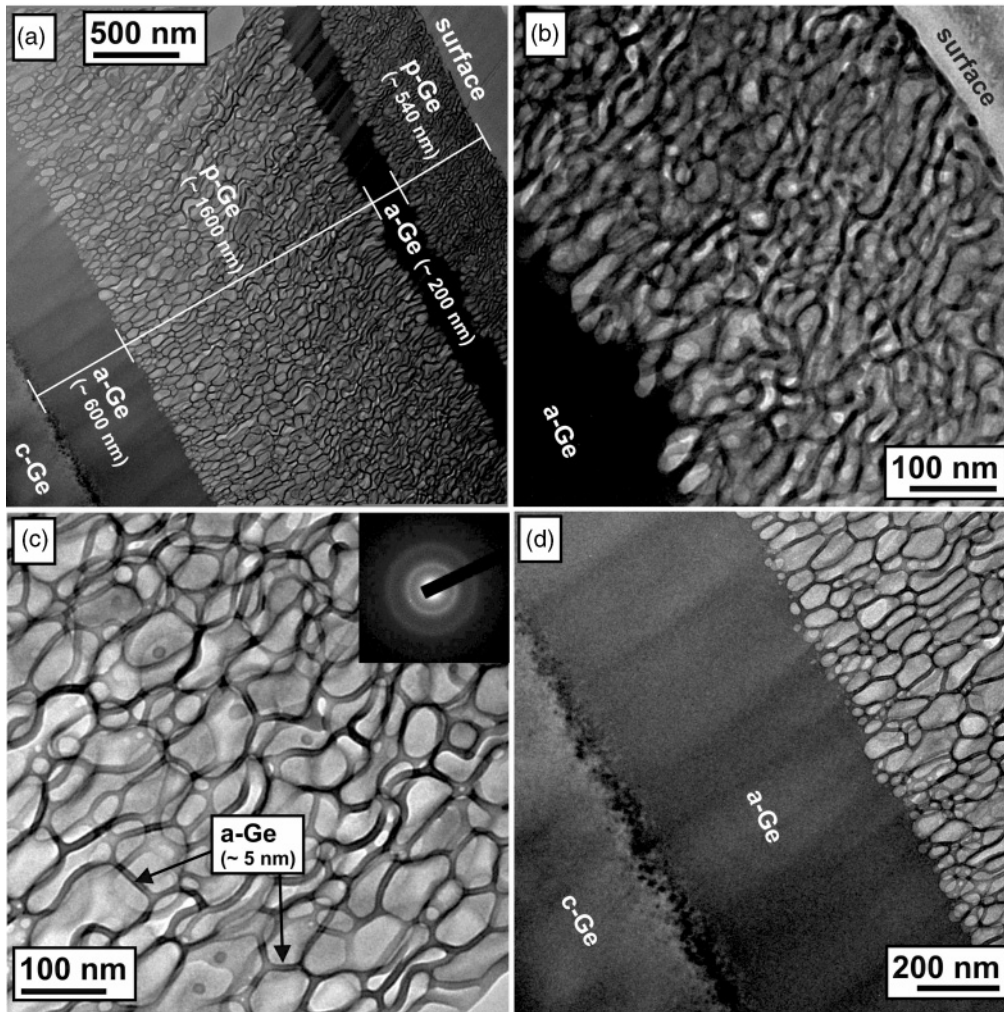
FIG. 6. The cs-TEM image of the complete porous layer structure is shown in (a) for room temperature irradiated germanium with 3 MeV I, $\Theta = 7°$ and an ion fluence of 4.0×10^{16} cm^{-2}. In addition, magnified views of the sharp transitions between (b) porous surface and amorphous interlayer, (c) the buried porous layer, and (d) the sharp transition between the buried porous layer and the underlying amorphous layer as well the crystalline substrate are depicted. The inset of (c) shows an electron diffraction pattern of a porous cell wall.

overestimate d_p for very thin layers which only consist of single voids.

A drastic modification at the surface becomes apparent in Fig. 7(b): A large hill-like surface structure was formed, which will be discussed in more detail by means of the following pv-SEM investigations. Compared to the atomically flat and featureless surface of a c-Ge sample, the pv-SEM images of samples irradiated with 1.2 and 2.5×10^{16} cm^{-2} (regions I and II), as depicted in Figs. 9(a) and 9(b), show for both regions a rough surface consisting of holes and hills with diameters of several nanometers. The observed craters are obviously the top view of the porous, columnar-shaped structure evident in the cs-SEM images (cf. Figs. 5 and 6). This suggests that the surface structure did not change significantly; it deepens only with increasing N_I. The intensive surface blackening can now be clearly attributed to the increased surface roughness. In region III, the surface structure changes drastically [Fig. 9(c)]. The entire surface is covered by a "worm-like" structure (in the following referred to as a "microstructure") with vertical dimensions of 200 to 700 nm and hill diameters of several

microns. This structure, once evolved, seems to be quite stable and does not change anymore with increasing N_I. The inset of Fig. 9(c) clearly displays a nanoporous surface structure on top of the microstructure, which is the same structure that has been found at lower fluences (regions I and II). The micrometer-sized surface structure in region III corresponds to the modified sample color (see Table II).

As mentioned above, even for the highest ion fluence, the appearance did not change in the case of the irradiation at $\Theta = 45°$ compared to the irradiation at $\Theta = 7°$ (cf. Table II). The reason becomes evident in cs- and pv-SEM images as shown in Fig. 10. For samples irradiated at $\Theta = 45°$ with ion fluences within region III, the same nanoporous surface structure has been found like in regions I and II [inset of Fig. 10(b), pv-SEM], but no worm-like microstructure could be detected at the surface [Fig. 10(b)]. Instead, compared to the irradiation at $\Theta = 7°$ (cf. Fig. 6), Fig. 10 a shows a tendency of alignment of the porous structure, which may be due to movement of the layer into the direction of the ion beam projection onto the sample surface [arrows in Fig. 10(a)]. This
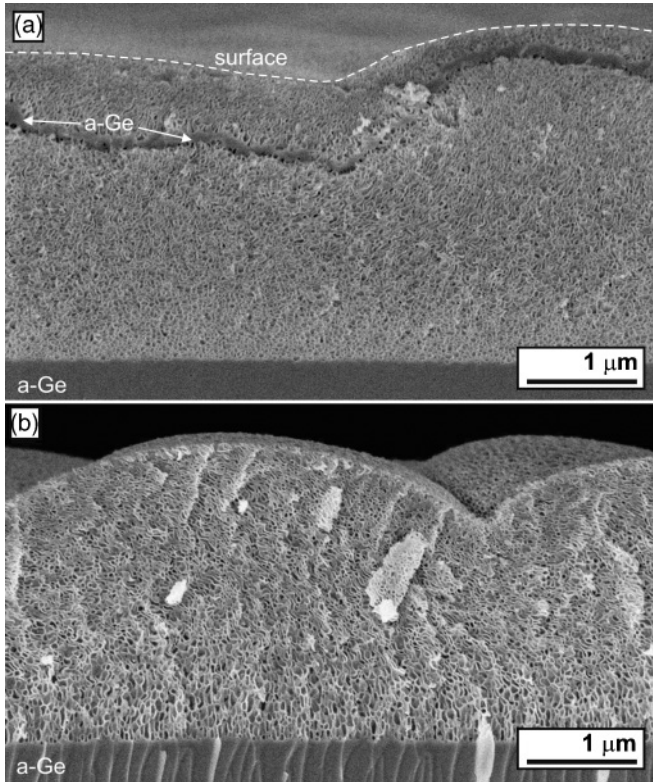
FIG. 7. Cs-SEM images of samples irradiated with 3 MeV I, $\Theta = 7°$ demonstrates the decrease of the amorphous interlayer [(a), $N_I = 5.0 \times 10^{16}$ cm^{-2}] until the surface and buried layer have merged into a single porous structure [(b), $N_I = 7.0 \times 10^{16}$ cm^{-2}]. Also, the formation of a large hill-like structure can be seen in (b).
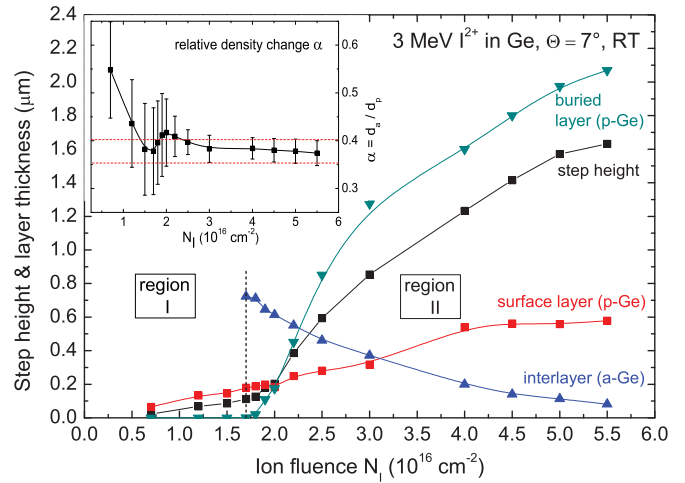

FIG. 8. (Color online) Step height Δz as well as porous and amorphous layer thickness are shown for the irradiation of germanium with 3 MeV I, $\Theta = 7°$ as a function of the ion fluence N_I. The estimate of the relative change in density α is depicted in the inset.

is an indication of the formation process of the microstructure as being completely different compared to the void formation, which will be discussed in Sec. IV B.

The average roughness R_a determined by AFM profilometry for Ge irradiated with 3 MeV I under an angle of 7° and 45° is depicted in Fig. 11 versus N_I. The unirradiated Ge shows an atomically flat surface with $R_a < 1$ nm. For both, $\Theta = 7°$

and 45°, R_a increases rapidly with ongoing irradiation (region I) up to a value of about 5 nm. This coincides with the onset of blackening as a visual indication of roughness increase. At $N_I > 1.5 \times 10^{16}$ cm^{-2} (region II), R_a remains constant or decreases slightly within experimental uncertainty, even at the transition to region III. Since the sample underground is subtracted by a polynomic fit and the edge length of the scanned area is only 1 μm, the microstructure observed at $\Theta = 7°$ is not visible on this roughness scale. Thus, only nanometer-sized roughness features are detected and found to be the same in regions II and III (i.e., independent of Θ). This is in good agreement with the pv-SEM image data [cf. inset of Figs. 9(c) and 10(b)]. The measured surface roughness also agrees with the results of Kaiser et al.[48] with respect to the threshold fluences and the actual roughness values. The linear increase reported there is also found in our experiments for fluences within region I, which corresponds to the fluence range examined by Kaiser.[48]
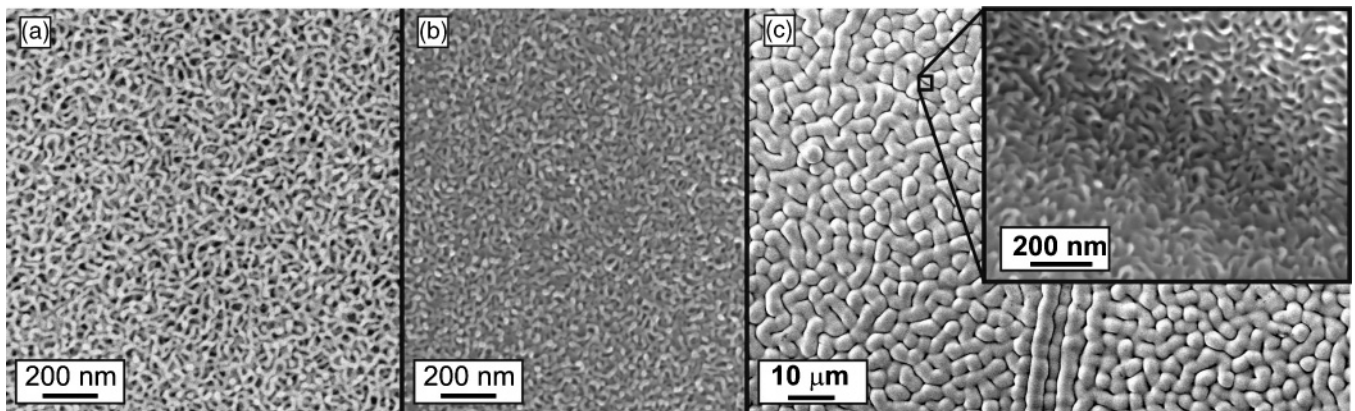

FIG. 9. Pv-SEM of the samples irradiated with 3 MeV I, $\Theta = 7°$ and an ion fluence of 1.2×10^{16} cm^{-2} [(a), region I] and 2.5×10^{16} cm^{-2} [(b), region II] show the same rough porous surface for both regions. For the irradiation of germanium with an ion fluence of 5.5×10^{16} cm^{-2} (region III), the pv-SEM image revealed that the entire surface is covered by a "worm-like" structure with diameters of several microns. The inset of (c) displays a magnification, which exhibits a nanoporous surface structure on top of the microstructure, with the same appearance as observed in regions I and II [cf. (a) and (b)].
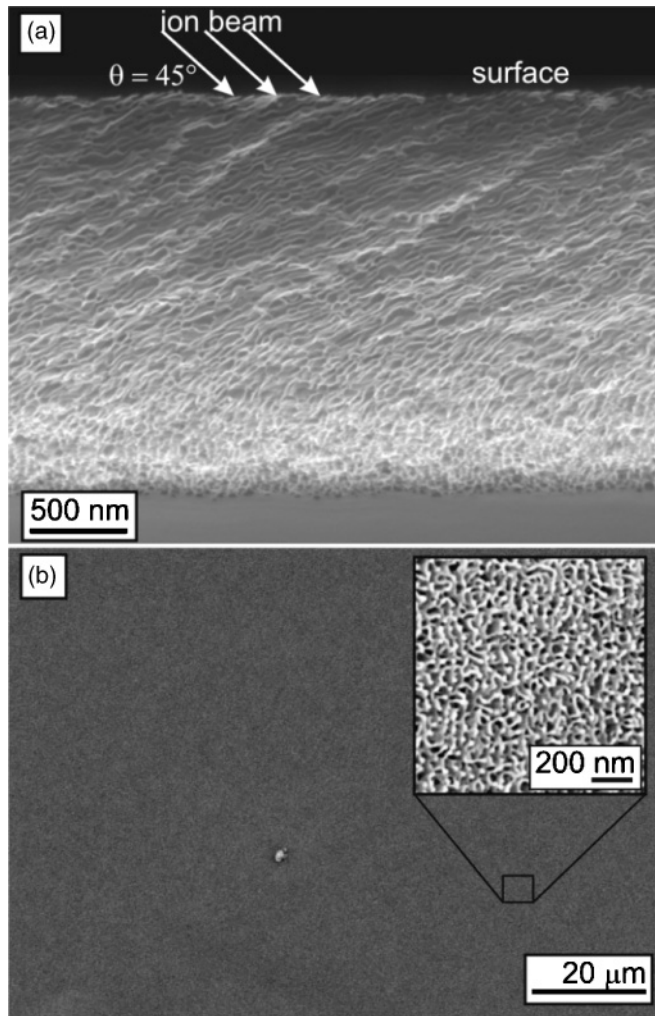
FIG. 10. (a) For samples irradiated with 3 MeV I, $\Theta = 45°$, and ion fluences in region III, a movement of the porous layer into the direction of the ion beam projection is visible in the cs-SEM. The pv-SEM in (b) revealed the existence of a nanoporous surface structure similar to Fig. 9(c) (irradiation with $\Theta = 7°$), but without the formation of a microstructure.

Structural analysis of Au and Ag irradiated samples with SEM at low N_I revealed a nanoporous, columnar-shaped structure at the surface, which is very similar to iodine irradiations within region I. With ongoing Au-ion irradiation, this porous surface structure expands into the depth *without* the formation of buried voids as illustrated in Fig. 12(a) for $N_I = 2.0 \times 10^{16}$ cm^{-2}. In contrast to all iodine irradiations, no buried porous layer is formed for all N_I used. The irradiation with Au ions only leads to an extreme expansion of the porous surface layer with increasing N_I [cf. Fig. 12(b)]. Despite the difference, the whole porous structure has a similar shape, wall thickness, and dimension of voids for the irradiation with I and Au. In addition, the factor α was estimated to be 0.38 and 0.44 for Au and Ag irradiation, respectively. These values are in good agreement with the calculated values for the iodine irradiations. Moreover, in the case of Au-ion irradiation, the microstructure formation sets in at $N_I = 5.5 \times 10^{16}$ cm^{-2}, which agrees well with the observed change in sample appearance from black to matte and silvery.
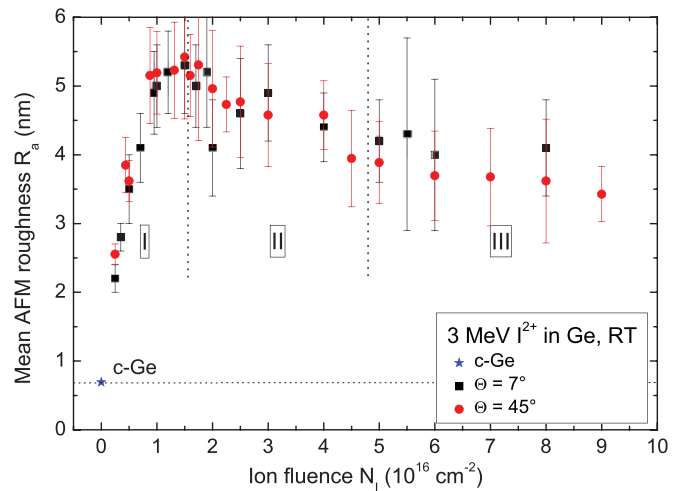

FIG. 11. (Color online) Average roughness of the surface R_a of germanium irradiated with 3 MeV I under an angle of $\Theta = 7°$ and $45°$, respectively, as a function of the ion fluence N_I. The three regions are indicated by dotted lines.

The microstructure has a diameter of several microns and does not change once it evolved, similar to the I irradiation.

3. Effects on void formation at LNT

The step heights Δz as a result of swelling are shown in Fig. 13(a) as a function of N_I for Ge irradiated at LNT with 3 MeV I under an angle of $\Theta = 7°$ and $\Theta = 45°$ in comparison to the corresponding RT irradiations. The increased Δz at LNT irradiation for N_I in the range of 1 to 3 $\times$ 10^{16} cm^{-2} (e.g., $\Delta z = 38$ nm for $N_I = 1.0 \times 10^{16}$ cm^{-2}) may be attributed to amorphization-induced volume expansion Δz^{am} (cf. Sec. III A). This is confirmed by SEM investigations, which show no voids or porous structure within the amorphous layer. A strong volume expansion caused by void formation is only observed for LNT irradiation with $N_I > 3 \times 10^{16}$ cm^{-2}. However, Fig. 13(a) illustrates that at LNT Δz is much smaller than at RT and it is not possible to identify three regions as for RT irradiation. Moreover, the surface color of the sample exhibits a different appearance compared to RT irradiation. Samples irradiated in a fluence range of 1 to 6 $\times 10^{16}$ cm^{-2} showed a shiny, silvery surface like c-Ge, which changed to a bright-silvery, matte appearance for $N_I > 6 \times 10^{16}$ cm^{-2}.

An explanation may be given by the cs- and pv-SEM images shown in Fig. 13 for the LNT irradiation with fluences of 5 [Fig. 13(b)] and 8 $\times 10^{16}$ cm^{-2} [Fig. 13(c)]. Compared to RT irradiations (cf. Figs. 5 and 6), no porous layer can be seen at the surface, which is still amorphous and free of voids consistent with the fact that no significant blackening was observed. The suppression of a porous surface layer may explain the missing increase in Δz at low ion fluences (region I). However, the formation of a buried porous layer as seen in in Fig. 13(b) causes the increased Δz at high ion fluences. Furthermore, even at high N_I [Fig. 13(c)] only isolated spherical voids are formed with sizes in the range of 10 to 30 nm. Hence, smaller void dimension and the absence of a porous surface layer (region I) lead to a lower saturation value of Δz for LNT compared to RT irradiations. Nevertheless, the
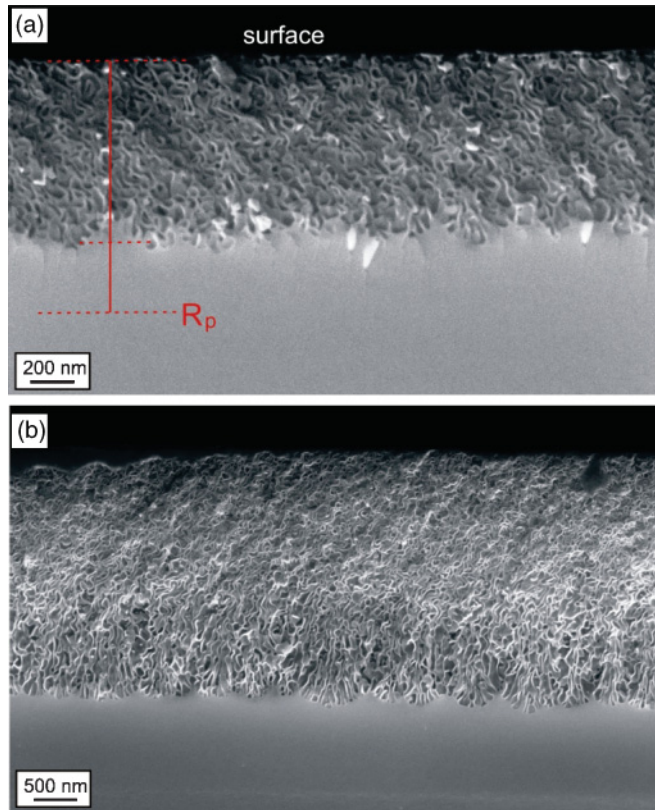
FIG. 12. (Color online) Cs-SEM images of Au irradiated Ge samples showing the formation [(a), $N_I = 2.0 \times 10^{16}$ cm^{-2}] and growth [(b), $N_I = 5.0 \times 10^{16}$ cm^{-2}] of a porous surface layer.

buried porous layer has been formed in the depth of R_p (not shown).

With ongoing irradiation at LNT and $\Theta = 7°$ the formation of a microstructure at $N_I = 5 \times 10^{16}$ cm^{-2} is clearly visible [insets in Fig. 13(b)], which obviously enables void formation within these microstructures and at the surface at higher ion fluences [Fig. 13(c), $N_I = 8 \times 10^{16}$ cm^{-2}]. In comparison to a sample irradiated at RT [e.g., Fig. 9(c)], the microstructures resemble one another in shape and dimension. This leads to the conclusion that the formation of such a structure is independent of the existence of a porous surface layer. Again, the formation fluence for the microstructure agrees with the observed change in sample appearance from shiny, silvery to a matte, silvery surface.

IV. DISCUSSION

A. Porous layer formation

RBS damage analysis of c-Ge samples irradiated with 3 MeV I at $\Theta = 7°$ and RT showed that the amorphization is reached at $N_I^{am} = 2 \times 10^{13}$ cm^{-2}. This agrees well with other work on defect formation in Ge due to ion irradiation.[49,50] At fluences two orders of magnitude above N_I^{am}, void formation in the a-Ge layer and its transformation into a sponge-like, porous structure was observed for all irradiation conditions used. Structural analysis with cs- and pv-electron microscopy delivered a consistent picture of porous layer formation
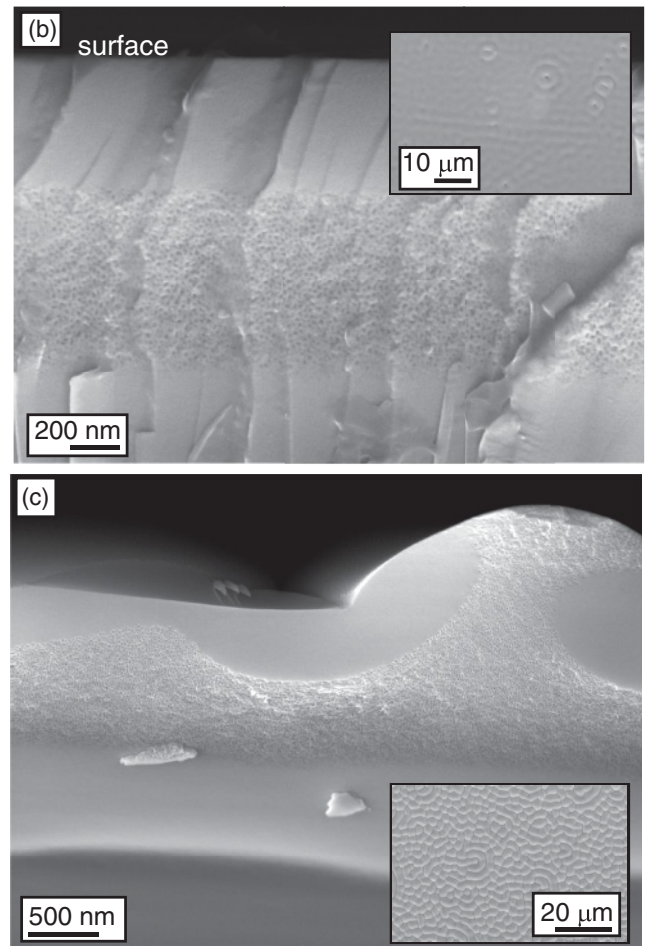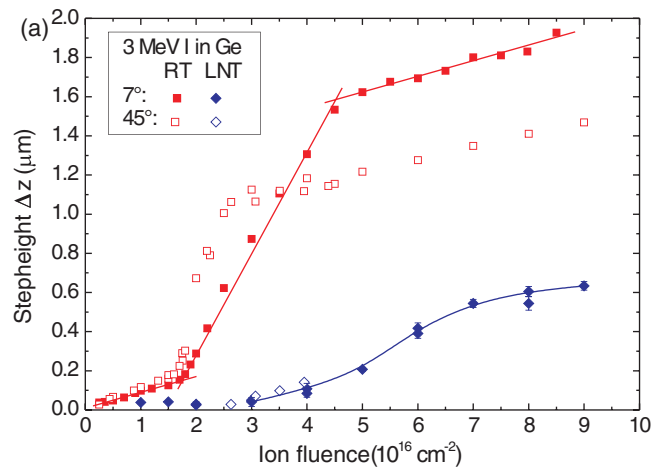

FIG. 13. (Color online) (a) Step heights Δz are shown as a function of ion fluence N_I for Ge irradiated at LNT with 3 MeV I under an angle of $\Theta = 7°$ and $45°$ in comparison with the corresponding RT irradiations. Cs-SEM images of these samples, (b, $N_I = 5.0 \times 10^{16}$ cm^{-2}) and (c, $N_I = 8.0 \times 10^{16}$ cm^{-2}), show the formation of a buried porous layer with isolated spherical voids. The pv-SEM images in the insets demonstrate (b) the onset and (c) the advanced stage of the microstructure formation.

with respect to irradiation fluence and allowed to connect macroscopic observations with microscopic effects. For all RT irradiations the developed porous structures are very similar in shape (i.e., wall thickness and cell dimension are in the same
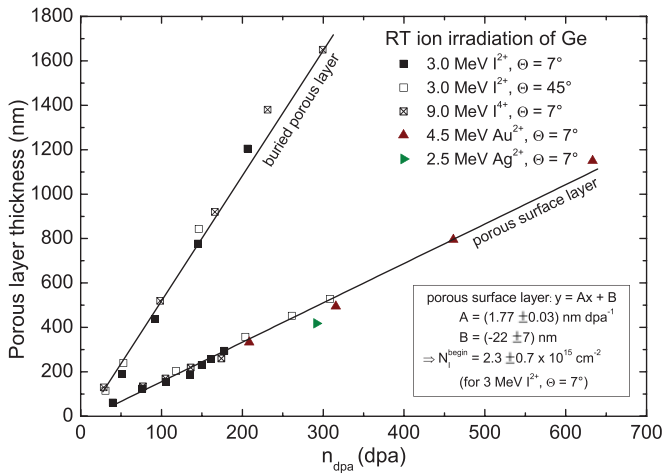
FIG. 14. (Color online) Thickness of the porous surface and the buried porous layer for germanium irradiated with different irradiation conditions as a function of the normalized ion fluence n_{dpa}. Data were fitted linearly (solid lines).

order of magnitude). Independent of energy deposition and ion species, the morphological changes begin at the surface with the formation of columnar porous structures, which increase into the depth with ongoing irradiation. In the near surface region the lateral volume expansion is mechanically constrained by the surrounding material which leads to a dominating expansion into the direction perpendicular to the surface. As a consequence, the voids at the surface enlarge into the z direction with increasing ion fluence and the characteristic columnar structure arises.

The higher irradiation energies in the range of several MeV, however, cause an energy deposition in a greater depth compared to previous work,[9–17] which results in the formation of an additional buried porous layer for the I irradiations (independent of the energy deposition and angle of incidence). Furthermore, the onset of buried void formation does not appear in the depth of the maximum of ϵ_n but rather in the depth of R_p. This leads to the conclusion that chemical properties of the irradiated ions are responsible for the formation or absence of a buried porous layer.

In Fig. 14, the thickness of the porous surface and buried porous layer is depicted as a function of the normalized ion fluence $n_{\text{dpa}} = (N_{\text{displ}}^a N_I)/N_0$. In this calculation, N_{displ}^a refers to the average value of N_{displ} over the thickness of the original amorphous material d_a that became porous during the irradiation. Additionally, for the calculation of n_{dpa} for the buried porous layer, N_I was subtracted by the value of the threshold fluence (see Table II), that is, $N_I = 0$ (consequently $n_{\text{dpa}} = 0$) corresponds to the threshold fluence where the void formation at R_p begins. It can be seen that despite the different ion species, different energy depositions, and directions of incidence, the slope of the thickness of both porous layers is only a function of n_{dpa}, which implies that the volume expansion is determined solely by ϵ_n. Furthermore, the porous layer thickness linearly depends on n_{dpa}. The extrapolation of the regression line for the porous surface layer reveals the existence of an energy deposition threshold of about $n_{\text{dpa}} = 12.4 \pm 4.2$, above which void formation begins in

a-Ge under heavy-ion irradiation at RT. As an example, in the case of the ion irradiation with 3 MeV I and $\Theta = 7°$ $N_{\text{displ}} = 2.3$ Å^{-1} ion^{-1} at the surface), a threshold fluence of $2.3 \pm 0.7 \times 10^{15}$ cm^{-2} can be calculated, which agrees well with the onset of the volume expansion and the surface appearance change (cf. Table II).

SHI experiments showed that electronic energy deposition is well capable of inducing porosity in a-Ge as well. Nevertheless, ϵ_e can be excluded as the main reason for porous layer formation for heavy ion irradiations because ϵ_e is one order of magnitude lower than the electronic energy deposition necessary for void formation[27] and because of its depth profile (cf. Fig. 1). The maximum of ϵ_e occurs at the surface, which is in contrast to the result that the thickness of the buried layer, once evolved, increases much faster than the porous surface layer. Indeed, the significant increase of the buried layer can be attributed to the higher ϵ_n in the depth of R_p compared to the surface (cf. Fig 1).

As suggested by different groups,[9–13] the energetically favorable agglomeration of vacancy-like defects plays an important role in the formation of the observed morphological changes in the amorphous phase. Our results confirm this assumption since the changes depend only on ϵ_n (cf. Fig. 14), which dominates the formation of vacancies and interstitials in the energy regime used. For crystalline materials (e.g., metals), void formation can be explained by the agglomeration of vacancies, which are generated during ion irradiation.[51,52] Such a high vacancy concentration can be achieved due to the presence of dislocations which effectively absorb the interstitial component of the Frenkel pairs. However, in amorphous materials, dislocations as the biased interstitial sink are absent.[53] Moreover, it is difficult to define Frenkel pair defects in amorphous materials. Nevertheless, MD simulations of an amorphous Lennard-Jones solid[54] show that ion irradiation is able to produce Frenkel pair-like defects. Simulations revealed that the interstitial-like defects disappear very rapidly by small positional rearrangements with their neighboring lattice atoms[54] or at interfaces[53] and leave the vacancies behind. These vacancies migrate and remain, if they escape recombination. In addition, a simulation performed for covalently bonded amorphous systems[55] showed that vacancies and small vacancy clusters are stable and do not diminish under static relaxations. The driving force for vacancy clustering in covalent solids may be a longer lifetime of vacancy like defects[54] and the elimination of dangling Ge bonds as proposed by Wang and Birtcher.[13] Therefore, the reduction of dangling bonds at void surfaces may be the main reason for the formation and the stability of these big vacancy clusters in a-Ge. Consequently, the formation of huge voids with dimensions of several nanometers may be attributed to a continuous growth of the small clusters as they act as sinks for vacancies produced thereafter.

If the formation process is governed by vacancy diffusion and clustering, the surface of the sample can be the main reason for the differences between surface and buried porous structure. As an interface, it is rich in defects and dangling bonds and can act as an effective sink for interstitials, whereas the remaining vacancies tend to energetically favorable agglomeration.[13,53] According to the model of Nitta,[56]

this effect of diffusion and vacancy clustering leads to a columnar-shaped structure. In the bulk material, where no effective sinks for the interstitial component of the Frenkel pair is available, the recombination of the Frenkel pair components dominate and no void formation can be observed. Recent computer simulation results of radiation-induced surface nanostructure formation in amorphous materials[57] are consistent with our experimental observations, which were achieved under comparable experimental conditions. This three-dimensional (3D) simulation takes account of the free energy of mixing and interfacial energy as well as considers the generation and elimination rates of vacancies, recombination with interstitials and redeposition of sputtered atoms. The morphological changes as well as the length scale of the simulated porous surface structures agree well with the experimental observations shown here and with the findings that were reported by other groups.[9–17]

A buried porous layer is formed for all iodine irradiations in the depth of R_p at high N_I [i.e., in a depth region where the iodine concentration is very high (several atom percent)]. Thus, this depth can be regarded as an interface, which is rich in defects such as I interstitials and vacancies and consequently contains many dangling bonds.[53] Similar to the void formation at the surface, the agglomeration of vacancies to minimize dangling Ge bonds at void surfaces may be the driving mechanism. In the case of Au ion irradiation, no buried porous layer could be found, even though a high Au impurity concentration should also exist at R_p. Au diffusion in Ge investigated at low temperature by lifetime measurements and laser mass spectrometry shows that Au becomes localized in a lattice site, if the Au ion encounters a vacancy[58] and consequently is bonded to Ge atoms. This leads to a reduction of the vacancy concentration as well as the number of dangling bonds of the Ge atoms. Furthermore, investigations on Au-doped Ge clusters demonstrate that dangling bonds of Ge atoms are completely eliminated by the encapsulation of the Au atom in the Ge matrix.[59] Hence, in a-Ge, which has still a short-range order that is quite well defined,[60,61] the diffusion of Au (and Ag) by an interstitial mechanism[62,63] and the final localization in a lattice site reduces dangling bonds and consequently inhibits the formation of stable vacancy clusters in the depth around R_p.

As discussed in Sec. III B, thermally induced defect mobility seems to play an important role in porosity formation. At LNT, the volume expansion does not increase until a threshold fluence of $N_I = 3.5 \times 10^{16}$ cm^{-2} is reached and Δz is much smaller than at RT irradiation. The reason is the limited mobility of the irradiation-induced Frenkel pairs at LNT. For low temperatures, the formation of voids caused by vacancy clustering is shifted toward higher ion fluences because the vacancies are not as mobile as they are at RT. Consequently the void dimensions are smaller for LNT compared to RT irradiation. This dependence on the irradiation temperature agrees with the results of Ottaviano,[24] who found a temperature-dependent increase of void dimensions and layer thickness from RT up to 513 K. This indicates that enhanced thermally induced defect mobility leads to a stronger volume expansion. Furthermore, similar to the results of Stritzker,[14] no blackening of the irradiated surfaces and consequently no voids or porous layer formation at the surface, was observed for

the irradiation at LNT. However, in contrast to these findings, a significant volume expansion caused by the formation of a buried porous layer occurred. The irradiation with 1 MeV Ge ions, as performed by Stritzker,[14] results in an energy deposition in a depth which is comparable to the iodine irradiations. However, the implanted Ge ions (interstitials) disappear by small realignments with their neighbors. Hence, even at high fluences the irradiation with Ge ions is not able to produce a buried porous layer according to the formation process proposed above.

Obviously, the formation of a porous surface layer is suppressed at LNT ion irradiations. A possible explanation may be the adsorption of atoms or molecules (e.g., hydrogen or oxygen) on the sample surface during the cooling of the sample, which leads to a reduction of surface defects and dangling Ge bonds. Consequently, the surface cannot act as an effective sink for interstitials anymore. This enables the recombination of the Frenkel pair components near the surface similar to the process in the bulk material. Furthermore, Ridgway[64] reported for ion irradiation at LNT that Frenkel defects may be preferably accommodated via three- and five-fold coordinated atoms instead of vacancy clustering. Thus, both effects, the dramatically reduced thermal mobility of defects and the Frenkel pair recombination or formation of three- and five-fold coordinated Ge-atoms, inhibit vacancy clustering and therefore suppress void formation at the surface at LNT irradiation. The defect- and impurity-rich buried layer still favors vacancy clustering to reduce dangling bonds, even at reduced thermal vacancy mobility, which leads to smaller void dimensions.

B. Plastic deformation

As mentioned in Sec. III B 2, the microstructure at the surface observed for all perpendicular irradiations ($\Theta = 7°$) at high ion fluences ($N_I > 5.0 \times 10^{16}$ cm^{-2}) has lateral dimensions of several microns, which is three orders of magnitude above the nanocavity diameters. This indicates a completely different formation process of this structure than of the void formation. In fact, ion irradiation causes a lot of mechanical stress within the irradiated a-Ge layer. The microstructure may thus be a result of stress reduction rather than a defect mobility-driven phenomenon. Electron microscopy investigations of samples irradiated at $\Theta = 45°$ (cf. Fig. 10), where no microstructure at the surface is formed, confirm this assumption. In this case, a movement of the amorphous layer (in the following referred to as surface shift) into the direction of the ion beam projection on the sample surface was observed.

Such shifts of amorphous surface layers are well known from SHI irradiations, where they occur if a material-specific electronic energy deposition threshold ϵ_e [ϵ_e approximately 12 keV nm^{-1} for Ge (Ref. 27)] is exceeded.[65,66] Hence, during perpendicular SHI irradiation a thin amorphous sample grows perpendicular and shrinks parallel to the ion beam, which is known as the ion hammering effect.[65,67,68] When the deformation is mechanically constrained by an inert surrounding (e.g., thin amorphous layer on bulk material), in-plane stress occurs. This prevents a deformation under normal ion incidence, whereas off-normal irradiations (e.g.,

$\Theta = 45°$) lead to a plastic flow into the direction of the projection of the ion beam at the surface. Plastic deformation during SHI irradiation maintains the macroscopic volume and was described by the modified viscoelastic Maxwell model.[69–72] The viscoelastic model by Trinkaus and Ryazanov[73] and Trinkaus[74–77] is a well established approach to explain the underlying ion-solid interaction. Based on this model, the surface shift $\Delta x(z = 0)$ is extracted as follows:

$$\Delta x = 3A_0(\epsilon_e)d_a N_I \sin(2\Theta), \qquad (4)$$

where $A_0(\epsilon_e)$ refers to the deformation yield as a function of ϵ_e and d_a is the thickness of the amorphous layer. Obviously, in the experiments done in the present paper, ϵ_e is too low (cf. Table I) to cause such an effect in the amorphous layer. Nevertheless, in the case of a-Si, it was reported that electronic energy deposition far below the threshold of $\epsilon_e = 14.2$ keV/nm (Ref. 66) is capable of inducing plastic deformation.[78,79] Hence, a similar process may be present for the irradiation of Ge in the MeV regime, because the orientation of the porous structure in Fig. 10 reflects the ion-beam-induced plastic flow process directly (i.e., a surface shift), similar to how it was demonstrated in SHI irradiated a-Ge recently.[27]

Furthermore, samples irradiated at LNT ($\Theta = 45°$) with its high threshold fluence of 3.5×10^{16} cm^{-2} for void formation (cf. Sec. III B3), provide another direct evidence for this assumption. Profilometric measurements of these samples (see inset of Fig. 15) revealed a dike formation at the boundary to the unirradiated material. With increasing N_I, the dike grows in size. Such a dike formation was observed for SHI irradiations at $\Theta = 45°$ as a direct consequence of the plastic deformation (i.e., the lateral mass transport into the direction of the ion beam projection.[72,80]). Thus, the cross section of the dike F_d has to be on a par with the laterally transported matter in the central region F_c since the plastic deformation process proceeds without material loss. The cross section F_c can be estimated by the integration of
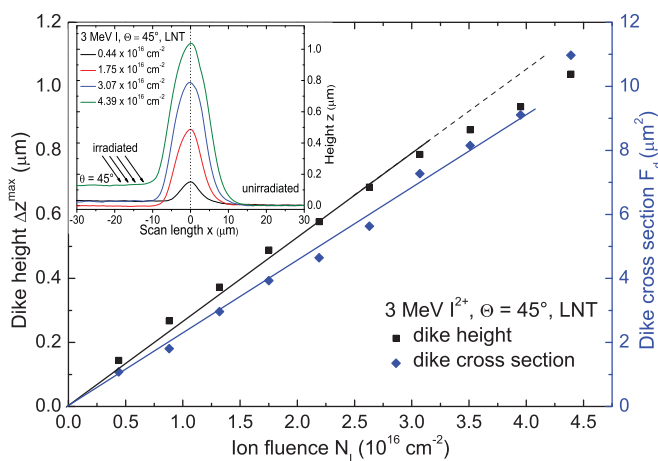
the observable surface shift $\Delta x(z)$ over the total deformation depth d_a according to the following formula (see also Ref. 80):

$$
\begin{aligned}
F_c &= \int_{d_a}^{0} \Delta x(z)dz = \frac{3}{2}A_0(\epsilon_e)d_a^2 N_I \sin(2\Theta) \\
&= \frac{d_a}{2}\Delta x(z=0) = \lambda N_I \overset{!}{=} F_d.
\end{aligned} \qquad (5)
$$

According to Eq. (5), the cross section of the dikes F_d has to be a linear function of the ion fluence. This is confirmed by Fig. 15, where F_d as well as the dike height is depicted as a function of N_I. It can be clearly seen that F_d increases linearly with increasing N_I. Moreover, no incubation fluence is observed, the extrapolation of the regression line crosses the point of origin similar to the observed surface shift Δx for SHI irradiations.[66] In contrast, no dike formation is observed for the irradiations at $\Theta = 7°$.

To summarize, even for the irradiation with ion energies of several MeV, a detectable plastic deformation process in a-Ge takes place. In the case of the irradiation at $\Theta = 45°$, a plastic flow of the amorphous surface occurs even at low N_I, leading to a mechanical in-plane stress reduction. For perpendicular ion incidence ($\Theta = 7°$), however, the deformation is mechanically constrained by the bulk material, thus, in-plane stresses build up which cannot be reduced by a plastic flow process. In this case, the mechanic stress seems to be reduced at high N_I by the formation of a microstructure at the sample surface.

V. SUMMARY

The influence of different irradiation parameters on void formation in heavy-ion irradiated amorphous Ge surface layers was investigated. For all irradiation parameters a strong swelling of the irradiated material was observed caused by the formation and growth of voids. This leads to a gradual transformation of the amorphous layer into a sponge-like porous structure. Independent of energy deposition and ion species, the morphological changes begin close to the surface with the formation of a columnar porous structure for room temperature irradiation at ion fluences two orders of magnitude above the amorphization threshold. With ongoing I-ion irradiation, buried voids are formed independent of the energy deposition and angle of incidence. We demonstrated that the onset of buried void formation does not appear in the depth of the maximum of ϵ_n, but rather in the depth of the projected ion range. In contrast to the I-ion irradiation the irradiation with Au and Ag ions solely results in the formation and expansion of a porous surface layer. We showed for all room temperature irradiations that the volume expansion depends linearly on the value of ϵ_n despite the different ion species, different energy depositions, and directions of incidence. This clearly demonstrates that the structural changes are determined solely by the nuclear energy deposited within the amorphous phase. Hence, the whole mechanism which leads to the observed structural changes was discussed based on the approach of energetically favorable agglomeration of ion-induced vacancy-like defects caused by ϵ_n. Based on this mechanism and the fact that buried voids are formed in the depth of the projected ion range, we conclude that chemical properties of the irradiated ions are responsible for the formation or absence

FIG. 15. (Color online) Dike height Δz^{max} and dike cross section F_d for germanium irradiated with 3 MeV I at LNT and under an angle of $\Theta = 45°$ as a function of ion fluence N_I. Data were fitted linearly (solid lines). Additionally, the inset illustrates the dike formation for nonperpendicular ion irradiation of germanium as measured by the surface profilometer.

of a buried porous layer. Low temperature I-ion irradiation demonstrated that thermally reduced defect mobility plays an important role in void and porous layer formation because small isolated spherical voids were formed only in the depth of R_p.

In addition, at high ion fluences all perpendicular ion irradiations lead to a formation of a microstructure at the surface, whereas for nonperpendicular ion irradiation a nonsaturating irreversible plastic deformation (ion hammering) without a microstructure formation is observed. The effect of plastic deformation shows a linear dependence on the ion fluence similar to how it was observed for many materials

irradiated with SHIs. Finally, we provide an explanation for the differences in surface morphology observed for different angles of incidence of the ion beam.

[1] R. Callec, P. N. Favennec, M. Salvi, H. L. Haridon, and M. Gaunea, Appl. Phys. Lett. **59**, 1872 (1991).

[2] R. Callec, A. Poudoulec, M. Salvi, H. L. Haridon, P. N. Favennec, and M. Gaunea, Nucl. Instrum. Methods Phys. Res. Sect. A **80/81**, 532 (1993).

[3] N. Nitta, M. Taniwaki, T. Suzuki, Y. Hayashi, Y. Satoh, and T. Yoshiie, Materials Transactions **43**, 674 (2002).

[4] S. M. Kluth, J. D. F. Gerald, and M. C. Ridgway, Appl. Phys. Lett. **86**, 131920 (2005).

[5] C. C. Jacobi, T. Steinbach, and W. Wesch, Nucl. Instrum. Methods Phys. Res. Sect. B (in press).

[6] G. Destefanis and J. Gailliard, Appl. Phys. Lett. **36 (1)**, 40 (1980).

[7] M. Shaanan, R. Kalish, and V. Richter, Nucl. Instrum. Methods Phys. Res. Sect. B **7/8**, 443 (1985).

[8] S. Kluth, D. Llewellyn, and M. C. Ridgway, Nucl. Instrum. Methods Phys. Res. Sect. B **242**, 640 (2006).

[9] I. H. Wilson, J. Appl. Phys. **53**, 1698 (1982).

[10] B. R. Appleton, O. W. Holland, J. Narayan, O. E. Schow, J. S. Williams, K. T. Short, and E. Lawson, Appl. Phys. Lett. **41**, 711 (1982).

[11] O. W. Holland, B. R. Appleton, and J. Narayan, J. Appl. Phys. **54**, 2295 (1983).

[12] B. R. Appleton, O. W. Holland, D. B. Poker, J. Narayan, and D. Fathy, Nucl. Instrum. Methods Phys. Res. Sect. B **7/8**, 639 (1985).

[13] L. M. Wang and R. C. Birtcher, Philos. Mag. A **64**, 1209 (1991).

[14] B. Stritzker, R. G. Elliman, and J. Zou, Nucl. Instrum. Methods Phys. Res. Sect. B **175–177**, 193 (2001).

[15] T. Janssens, C. Huyghebaert, D. Vanhaeren, G. Winderickx, A. Satta, M. Meuris, and W. Vandervorst, J. Vac. Sci. Technol. B **24**, 510 (2006).

[16] J. Yanagisawa, K. Takarabe, K. Ogushi, K. Gamo, and Y. Akasaka, J. Phys. Condens. Matter **19**, 445002 (2007).

[17] L. Romano, G. Impellizzeri, M. Tomasello, F. Giannazzo, C. Spinella, and M. Grimaldi, J. Appl. Phys. **107**, 084314 (2010).

[18] G. Kaltsas and A. G. Nassiopoulou, Sensors and Actuators A: Physical **76**, 133 (1999).

[19] S. C. Bayliss, P. J. Harris, L. D. Buckberry, and C. Rousseau, J. Mater. Sci. Lett. **16**, 737 (1997).

[20] H. Föll, J. Carstensen, and S. Frey, J. Nanomat. **2006**, 1 (2006).

[21] S. Gold, K.-L. Chu, C. Lu, M. Shannon, and R. Mase, J. Power Sources **135**, 198 (2004).

[22] K. Busch, *Photonic Crystals: Advances in Design, Fabrication, and Characterization* (Wiley-VCH, Weinheim, 2004).

[23] D. Sun, A. Riley, A. Cadby, E. Richman, S. Korlann, and S. Tolbert, Nature (London) **411**, 1126 (2006).

[24] L. Ottaviano, A. Verna, V. Grossi, P. Parisse, S. Piperno, M. Passacantando, G. Impellizzeri, and F. Priolo, Surf. Sci **601**, 2623 (2007).

[25] H. Huber, W. Assmann, R. Grötzschel, H. D. Mieskes, A. Mücklich, H. Nolte, and W. Prusseit, Mater. Sci. Forum **248–249**, 301 (1997).

[26] W. Wesch, C. S. Schnohr, P. Kluth, Z. S. Hussain, L. L. Araujo, R. Giulian, D. J. Sprouster, A. P. Byrne, and M. C. Ridgway, J. Phys. D: Appl. Phys. **42**, 115402 (2009).

[27] T. Steinbach, C. S. Schnohr, P. Kluth, R. Giulian, L. L. Araujo, D. J. Sprouster, M. C. Ridgway, and W. Wesch, Phys. Rev. B **83**, 054113 (2011).

[28] K. Gärtner, J. Jöhrens, T. Steinbach, C. S. Schnohr, M. C. Ridgway, and W. Wesch, Phys. Rev. B **83**, 224106 (2011).

[29] J. F. Ziegler, J. P. Biersack, and U. Littmark, *The Stopping and Range of Ions in Solids* (Oxford, Pergamon, 2003).

[30] K. Gärtner, Nucl. Instrum. Methods Phys. Res. Sect. B **132**, 147 (1997).

[31] K. Gärtner, Nucl. Instrum. Methods Phys. Res. Sect. B **227**, 522 (2005).

[32] W. Wesch, A. Kamarou, and E. Wendler, Nucl. Instrum. Methods Phys. Res. Sect. B **225**, 111 (2004).

[33] J. Gibbons, IEEE **60**, 1062 (1970).

[34] F. Morehead and B. Crowder, Radiat. Eff. **6**, 27 (1970).

[35] J. Dennis and E. Hale, J. Appl. Phys. **49**, 1119 (1978).

[36] G. Carter and R. Webb, Radiat. Eff. Lett. **43**, 19 (1979).

[37] R. Webb and G. Carter, Radiat. Eff. **59**, 69 (1981).

[38] N. Hecking, K. Heidemann, and E. Kaat, Nucl. Instrum. Methods Phys. Res. Sect. B **15**, 760 (1986).

[39] S. Campisano, S. Coffa, V. Rainieri, F. Priolo, and E. Rimini, Nucl. Instrum. Methods Phys. Res. Sect. B **80–81**, 514 (1993).

[40] K. Nordlund, M. Ghaly, R. S. Averback, M. Caturla, T. Diaz de la Rubia, and J. Tarus, Phys. Rev. B **57**, 7556 (1998).

[41] G. Impellizzeri, S. Mirabella, and M. Grimaldi, Appl. Phys. A **103**, 323 (2011).

[42] E. Wendler, Nucl. Instrum. Methods Phys. Res. Sect. B **267**, 2680 (2009).

[43] R. Temkin, W. Paul, and G. Connell, Adv. Phys. **22**, 581 (1973).

[44] K. Wang, W. Spitzer, G. Hubler, and E. Donovan, J. Appl. Phys. **57**, 2739 (1985).

[45] A. Witvrouw and F. Spaepen, J. Appl. Phys. **74**, 7154 (1993).

[46] G. Dalba, P. Fornasini, M. Grazioli, and F. Rocca, Phys. Rev. B **52**, 11034 (1995).

[47] M. Ridgway, C. Glover, G. de M. Azevedo, S. Kluth, K. Yu, and G. Foran, Nucl. Instrum. Methods Phys. Res. Sect. B **238**, 294 (2005).

[48] R. Kaiser, S. Koffel, P. Pichler, A. Bauer, B. Amon, A. Claverie, G. Benassayag, P. Scheiblin, L. Frey, and H. Ryssel, Thin Solid Films **518**, 2323 (2010).

[49] M. Hayes, A. Schroeter, E. Wendler, W. Wesch, F. Auret, and J. Nel, Physica B **404**, 4382 (2009).

[50] S. Decoster and A. Vantomme, J. Phys. D: Appl. Phys. **42**, 165404 (2009).

[51] S. Fisher and K. Williams, Radiat. Eff. Defects Solids **14**, 165 (1972).

[52] E. Kuramoto and T. Tsutsumi, J. Nucl. Mater. **212–215**, 175 (1994).

[53] V. Zhikharev and F. Batyrshin, MRS Symposium Proceedings: Modeling and simulation of thin-film Processing **389**, 155 (1995).

[54] T. K. Chaki and J. C. M. Li, Philos. Mag. B **51**, 557 (1985).

[55] P. Chaudhari, F. Spaepen, and P. Steinhardt, *Glassy Metals II* (Springer, Berlin, 1983).

[56] N. Nitta, M. Taniwaki, Y. Hayashi, and T. Yoshiie, J. Appl. Phys. **92**, 1799 (2002).

[57] K. Li, A. Bergquist, and L. Wang, Nucl. Instrum. Methods Phys. Res. Sect. B **267**, 3063 (2009).

[58] V. M. Matyushin, Tech. Phys. **44**, 804 (1999).

[59] X. Li and K. Su, Theor. Chem. Acc. **124**, 345 (2009).

[60] J. S. Lannin, N. Maley, and S. T. Kshirsagar, Solid State Communications **53**, 939 (1985).

[61] T. Hufnagel, Nat. Mater. **3**, 666 (2004).

[62] M. Millea, J. Phys. Chem. Solids **27**, 309 (1966).

[63] A. Strohm, S. Matics, and W. Frank, Defect Diffus. Forum **194–199**, 629 (2001).

[64] M. C. Ridgway, C. J. Glover, K. M. Yu, G. J. Foran, C. Clerc, J. L. Hansen, and A. N. Larsen, Phys. Rev. B **61**, 12586 (2000).

[65] S. Klaumünzer and G. Schumacher, Phys. Rev. Lett. **51**, 1987 (1983).

[66] A. Hedler, S. Klaumünzer, and W. Wesch, Nat. Mater. **3**, 804 (2004).

[67] S. Klaumünzer, M. D. Hou, and G. Schumacher, Phys. Rev. Lett. **57**, 850 (1986).

[68] M. D. Hou, S. Klaumünzer, and G. Schumacher, Phys. Rev. B **41**, 1144 (1990).

[69] S. Klaumünzer, Multisc. Phenom. Plast. Nato Science Series **367**, 441 (2000).

[70] S. Klaumünzer, Nucl. Instrum. Methods Phys. Res. Sect. B **225**, 136 (2004).

[71] A. Gutzmann, S. Klaumünzer, and P. Meier, Phys. Rev. Lett. **74**, 2256 (1995).

[72] A. Gutzmann and S. Klaumünzer, Nucl. Instrum. Methods Phys. Res. Sect. B **127/128**, 12 (1997).

[73] H. Trinkaus and A. I. Ryazanov, Phys. Rev. Lett. **74**, 5072 (1995).

[74] H. Trinkaus, J. Nucl. Mater. **223**, 196 (1995).

[75] H. Trinkaus, Nucl. Instrum. Methods Phys. Res. Sect. B **107**, 155 (1996).

[76] H. Trinkaus, J. Nucl. Mater. **246**, 244 (1997).

[77] H. Trinkaus, Nucl. Instrum. Methods Phys. Res. Sect. B **146**, 204 (1998).

[78] M. Chicoine, S. Roorda, L. Cliche, and R. A. Masut, Phys. Rev. B **56**, 1551 (1997).

[79] T. van Dillen, M. D. Dood, J. Penninkhof, A. Polman, S. Roorda, and A. Vredenberg, Appl. Phys. Lett. **84**, 3591 (2004).

[80] A. Hedler, S. Klaumünzer, and W. Wesch, Phys. Rev. B **72**, 054108 (2005).